J. Fluid Mech. (2008), *vol.* 604, *pp.* 99–123. © 2008 Cambridge University Press
doi:10.1017/S0022112008001006 Printed in the United Kingdom

Direct numerical simulations of a rapidly expanding thermal plume: structure and entrainment interaction

FRÉDÉRIC PLOURDE[1], MINH VUONG PHAM[1], SON DOAN KIM[1] AND S. BALACHANDAR[2]

[1]Laboratoire d'Etudes Thermiques, Ecole Nationale Supérieure de Mécanique et d'Aérotechnique, Téléport 2, 1 Avenue Clément Ader, BP 40109, 86961 Futuroscope Cedex, France

[2]Department of Mechanical and Aerospace Engineering, University of Florida, Gainesville, FL 32611-6250, USA

(Received 13 December 2006 and in revised form 5 February 2008)

We examine the development of a thermal plume originating from a localized heat source using direct numerical simulation. The Reynolds number of the plume, based on source diameter and the characteristic buoyancy velocity, is chosen to be 7700, which is sufficiently large so that the flow turns to a fully turbulent state. A highly resolved grid of 622 million points is used to capture the entire range of turbulent scales in the plume. Here at the source, only heat has been added with no mass or momentum addition and accordingly the vertical evolution of the mass, momentum and buoyancy fluxes computed from the simulation have been verified to follow those of a pure thermal plume. The computed vertical evolution of the time-averaged centreline velocity and temperature are in good agreement with available experimental measurements. Investigation of the time evolution of the plume shows periodic formation of vortex ring structure surrounding the main ascending column of hot fluid. The vortex ring forms very close to the heat source and even at formation it is three-dimensional. The vortex ring ascends with the plume and at an elevation of about two diameters it strongly interacts with and destabilizes the central column and subsequently a complex turbulent flow arises. Thus, relatively laminar, transitional and fully turbulent regimes of the plume evolution can be identified. In the fully turbulent regime, complex three-dimensional hairpin-like vortex structures are observed; but vestiges of the coherent vortex rolls that form close to the source can be observed in the turbulent statistics. It is shown that local entrainment consists of contraction and expulsion phases. Such instantaneous mechanisms drive the entrainment process, and the instantaneous entrainment coefficient shows large variation in both time and space with local values up to three times higher than the average entrainment level. Such findings support the view that entrainment mechanisms in plumes should be considered from an unsteady point of view. Movies are available with the online version of the paper.

1. Introduction

Buoyant plumes play a significant role in various fluid flows of environmental and technological importance. Accordingly, analytical, experimental and numerical works have been dedicated to the study of buoyant plumes. In the turbulent regime, buoyant plumes exhibit highly complex behaviour (Georges, Alpert & Tamanini 1997;

Bastiaans *et al.* 2000; Pham, Plourde & Doan 2005), which remains difficult to fully understand, analyse and predict. One of the main difficulties stems from the highly unstable nature of the flow, and the resulting rapid amplification of disturbances leading to abrupt transition (Nakagomeka & Hirata 1976). Such behaviour implicitly forces investigators to resort to detailed characterization through experimental measurements. For instance, Shabbir & George (1994) reported comprehensive measurements in a round buoyant plume that was generated by forcing a hot air jet up into a quiescent environment. Their experimental measurements, as well as those obtained by Nakagomeka & Hirata (1976) to quote just a few, allow us to compare experimental data with analytical theory. Taylor (1958) put forward the hypothesis that a turbulent buoyant element expands at the expense of the quiescent surrounding fluid through entrainment of exterior fluid. Morton, Taylor & Turner (1956) proposed similarity solutions of mean velocity and temperature in the turbulent region and Turner (1969) extended this analysis to plumes arising from a source of buoyancy.

The theoretical model of Morton *et al.* (1956) is based on a (virtual) point source assumption. However, as underlined by Fannelop & Webber (2003), while the point source model may suffice to describe plumes in regions high above the source, it is inadequate closer to a finite-sized heat source. Another limitation of the classic model is the use of the Boussinesq approximation, i.e. density variations are taken into account only in the buoyancy driving force. Rooney & Linden (1996) put forward the hypothesis that greater density differences primarily influence the plume radii, while the plume velocity is largely unchanged in comparison with the one obtained under the Boussinesq assumption. However, Fannelop & Webber (2003) suggest that such a result is strongly linked to the use of the Ricou & Spalding (1961) model. The general solutions obtained by Fannelop & Webber (2003) for their model plumes from finite-area sources exhibited a converging–diverging necking behaviour and were shown to be in reasonable agreement with the available experimental data from Liedkte & Schatzmann (1997) and Billeter & Fannelop (1989). However, it is important to point out that availability of accurate measurement close to a finite-sized heat source, either by detailed experiments or through numerical simulations, is essential to a more complete understanding of turbulent thermal plumes and their theoretical modelling.

The role of coherent structures in a turbulent plume and their relevance to the entrainment process have been actively investigated in recent years (Bhat & Narasimha 1996; Basu & Narasimha 1999). They conducted series of experiments as well as numerical simulations with jets and plumes subjected to volumetric heating to show that latent heat release plays a key role in local reduction of the entrainment rate. Sreenivas & Prasad (2000) established a model designed to explain thoroughly the main mechanisms inducing entrainment. Addition of off-source buoyancy creates a stable density stratification which resists the tendency of eddies to turn over. Their model demonstrates that, in the case of an ordinary plume wherein the addition of buoyancy is confined to the source, decreasing buoyancy along the downstream direction results in an unstable stratification and a baroclinic torque that enhances vorticity production. Cortese & Balachandar (1993) observed that in turbulent Rayleigh–Bénard convection, the thermal plumes are invariably spiralling. The spiralling nature of the plumes is due to vertical vorticity generated through a the breakage of axisymmetry and its intensification through a buoyancy-induced stretching mechanism.

Numerical simulations of jets and forced plumes are more common (Basu & Narasimha 1999; da Silva & Métais 2002) and comparatively speaking, computations of pure plumes are relatively limited. Stability of thermal plumes and their instability mechanisms have been investigated with two-dimensional simulations by Desrayaud &

Lauriat (1993). Bastiaans *et al.* (2000) carried out direct and large-eddy simulations of a pure thermal plume in a confined enclosure in order to highlight the transition phenomenon. They considered a planar plume that results from a line heat source. Numerical results obtained by Bastiaans *et al.* (2000) convincingly demonstrated that shortly after a symmetry-breaking bifurcation, three-dimensional structures do appear in the ascending flow.

Hunt & Kaye (2000) analysed the location of the asymptotic origin of positively buoyant turbulent plumes with a deficit of initial momentum flux. To characterize plumes, Hunt & Kaye (2000) introduced a source parameter $\Gamma \sim q_0^2 \phi_0 / f_0^{5/2}$ where q, f and ϕ are the mass, momentum and buoyancy fluxes while the subscript 0 refers to the source condition. Thus Γcorresponds to a measure of the relative importance of initial convective and thermal fluxes. Hunt & Kaye (2000) point out that plumes are classified as forced buoyant ($0 < \Gamma < 1$), pure plume ($\Gamma = 1$) or lazy ($\Gamma > 1$).

In this paper, we analyse the structure and statistics of a pure thermal plume from a finite-sized heat source under a turbulent regime. We will consider the axisymmetric configuration, where attention is focused on a conical plume resulting from a finite-sized circular heat source. The present work thereby complements the planar geometry studied by Bastiaans *et al.* (2000). Here the plume develops as a result only of heat release at the finite-sized source on the bottom boundary with no mass or momentum input. Consequently, the plume qualifies as a pure thermal plume. As we will see in § 3, the evolution of mass, momentum and buoyancy fluxes also satisfies the definition of a pure thermal plume (Hunt & Kaye 2000; Fannelop & Webber 2003). Our main objective in this study is to contribute to the detailed characterization of the near source region in the case of a finite-sized heat source. In addition, in the fully turbulent region, we focus attention on the role of coherent structures in driving the plume dynamics and the entrainment process. Aside from Basu & Narasimha (1999), no clear attention has been given to such structure–entrainment relationship. The results to be presented are for a modest Reynolds number of 7700, where the plume sufficiently above the source is subjected to a highly turbulent regime. A highly resolved grid of 622 million points is used in order to convincingly resolve all the relevant turbulent length scales.

Our paper is organized as follows. In § 2, we describe the problem, the governing equations and the boundary conditions. Numerical data obtained are described in detail in § 3. The main mechanism responsible for the destabilization of a pure thermal plume is analysed. Finally, an identification procedure is applied in order to highlight large-scale coherent structures that are located well above the source area and these structures are then related to the instantaneous plume entrainment. The identification of coherent structures has in fact allowed us to provide a plausible explanation for the pulsating behaviour recently observed experimentally in thermal plumes. Finally, conclusions are drawn in § 4.

2. Problem formulation

In this paper, we employ direct numerical simulation methodology to solve the low-Mach-number weakly compressible conservation equations of mass, momentum and temperature in a Cartesian coordinate system. The low-Mach-number approximation is often employed in the context of combustion and results in the filtering of the acoustic modes and the resulting equations are simpler than the fully compressible equations (Majda & Sethian 1985; Cook & Riley 1996; Lessani & Papalexandris

2006). The resulting equations are:

$$\frac{\mathrm{D}\rho}{\mathrm{D}t} + \rho\nabla\cdot\boldsymbol{u} = 0, \tag{1}$$

$$\rho\frac{\mathrm{D}\boldsymbol{u}}{\mathrm{D}t} = -\nabla p - (\rho - 1)\frac{\boldsymbol{e}_z}{Fr^2} + \frac{1}{Re}\nabla\cdot\boldsymbol{\sigma}, \tag{2}$$

$$\rho\frac{\mathrm{D}T}{\mathrm{D}t} = \nabla\cdot\left(\frac{1}{Re}\frac{\mu}{Pr}\nabla T\right). \tag{3}$$

In the above equations $\boldsymbol{u}$, p and $\boldsymbol{\sigma}$ correspond to the normalized velocity vector, pressure and viscous tensor, $\mathrm{D}/\mathrm{D}t$ is the substantial derivative operator, and $\boldsymbol{e}_z$ is a unit vector in the vertical direction. In our study, we have chosen the diameter of the circular heat source, D^*, as the length scale, the characteristic buoyant velocity of a fluid parcel, $U_0^* = \sqrt{g^*D^*(T_s^* - T_0^*)/T_0^*}$, as the velocity scale, D^*/U_0^* and $\rho_0^*U_0^{*2}$ as the time and pressure scales, where g^* is acceleration due to gravity. Normalized temperature T is defined as $T = (T^* - T_0^*)/(T_s^* - T_0^*)$, where T_s^* and T_0^* refer to the source and ambient temperature, respectively. Note that the asterisk refers to dimensional variables. The dimensionless parameters that appear in the governing equations are Reynolds number, $Re = \rho_0^*U_0^*D^*/\mu_0^*$, Froude number, $Fr = \sqrt{U_0^{*2}/D^*g^*}$, and Prandtl number, $Pr = \mu_0^*c_p^*/k_0^*$, in which ρ_0^*, μ_0^* and k_0^* correspond to density, viscosity and thermal conductivity, respectively, under ambient conditions. The numerical results to be discussed below were carried out for Re, Fr and Pr equal to 7700, 1.1 and 0.71, respectively. In the above equations non-dimensional density, ρ, and viscosity, μ, are obtained by normalizing by their ambient values, ρ_0^* and μ_0^*. The gas viscosity is taken to be a function of temperature following the Sutherland law, and is assumed to be a perfect gas. The variation in thermal conductivity and c_p^* is assumed to be such that Prandtl number remains a constant. Note that in the low-Mach-number assumption, viscous heating and adiabatic compression terms are neglected in the energy equation. As regards the present pure thermal plume, a local Grashof number can be defined in terms of dimensional distance above the heat source as $Gr(z^*) = (\rho_0^*/\mu_0^*)^2g^*z^{*3}(T_s^* - T_0^*)/T_0^*$ (Bill & Gebhart 1975). Based on the height of the computational domain, the largest local Grashof number (Bastiaans *et al.* 2000) for the present simulation can be estimated as 2.2×10^{10}, based on which we expect a fully turbulent flow field.

The governing equations were solved using a finite-difference method with staggered positioning of the variables in the computational grid. The spatial derivatives are approximated by second-order-accurate central-difference approximation. A second-order explicit Adams–Bashforth scheme was used for the time integration and a Poisson equation was solved for pressure. The Poisson equation was solved using fast Fourier transforms in the spanwise (y) and streamwise (z) directions and a tridiagonal matrix system in the final x-direction. The computational domain was chosen as $5D \times 5D \times 8D$ along the two horizontal and vertical directions, respectively, and was discretized using a highly resolved Cartesian fine mesh of $720 \times 720 \times 1200$ nodes. As the plume develops vertically, the region of intense turbulence is located off-axis, thus requiring fine resolution not only along to the axis, but over an extended cross-section around the axis. A Cartesian coordinate system with equi-spaced grid provides uniform resolution over the entire cross-section. The alternative to simulating a conical plume ascending above a cylindrical disk-shaped heat source is a cylindrical coordinate system. Urbin & Métais (1997), Zhou, Luo & Williams (2000) and Cantero *et al.* (2006, 2007) have successfully used rectangular Cartesian grids to simulate cylindrical jets, plumes and gravity currents.

In the present case, that of a pure thermal plume, the bottom boundary is considered to be a rigid no-slip no-penetration wall. At the centre of the bottom boundary is the hot disk of unit diameter which is maintained at unit non-dimensional temperature. The remaining bottom boundary is assumed to act as an adiabatic wall. The literature contains several studies devoted to turbulent forced plumes, where mass and momentum input is specified at the inflow. It has been established (George *et al.* 1977) that a forced plume can undergo transition from a laminar to a turbulent state with an abrupt breakdown of the potential core owing to rapid growth of disturbance (Bastiaans *et al.* 2000). However, fluctuations must be introduced in the inflow in order to promote transition (Urbin & Métais 1997; Stanley, Sarkar & Mellado 2001). As regards the pure thermal plume under study, to capture the fully turbulent behaviour observed in the experiments under similar conditions (Pham *et al.* 2006*a*) it is essential to introduce disturbance close to the heat source, for otherwise the flow will fail to transition within the computational domain and will remain unrealistically laminar. We disturb the flow with fluctuations added to the axial velocity component by superimposing a white noise disturbance to the velocity at the first nodes above the disk. The magnitude of disturbance added to the flow close to the heat source is an important parameter that controls the onset and location of transition. Several noise amplitudes were studied and the results presented here were obtained with a 5 % noise amplitude added to the vertical velocity component. At lower amplitudes of disturbance, the plume failed to become fully turbulent. At higher amplitudes of disturbance, the transition location advanced closer towards the source, but the characteristics of the fully turbulent region remained the same. A simple convective boundary condition was imposed at the side boundaries in order to allow entrainment and the convective boundary condition was also enforced at the top to allow passive advection of the vertical structures out of the computational domain without spurious reflection (Stanley *et al.* 2001; da Silva & Métais 2002).

The non-dimensional time step used in the computations is 2.5×10^{-3}, which satisfies both the stability and accuracy considerations. Initially, the flow is advanced about 40 non-dimensional time units to allow the initial transients to exit the domain. Once the statistically stationary state is established, time-averaged statistics are computed by averaging over 60 non-dimensional time units, which roughly corresponds to the formation of 20 thermally driven large-scale vortex formations. This allowed for an accurate description of the vortex formations and their complex development and interaction within the computational domain. A factor of particular importance is that the present grid and time step are adequate to resolve accurately the entire range of length and time scales down to the Kolmogorov scale (Stanley *et al.* 2001). Specific care was taken through *a posteriori* investigations to check the capacity of the proposed grid resolution to capture the smallest turbulent scales in the simulated flow. To assess resolution, we tested several grid resolutions and results from the highest resolution simulation are shown.

3. Results and Discussion

3.1. *Vicinity of finite-sized source*

First, it is essential to characterize the development of the ascending flow field from the finite-sized heat source at vertical positions well above the source. Figure 1 shows the radial profile of mean vertical velocity component, $\overline{u_z}$. All of them reveal a maximum

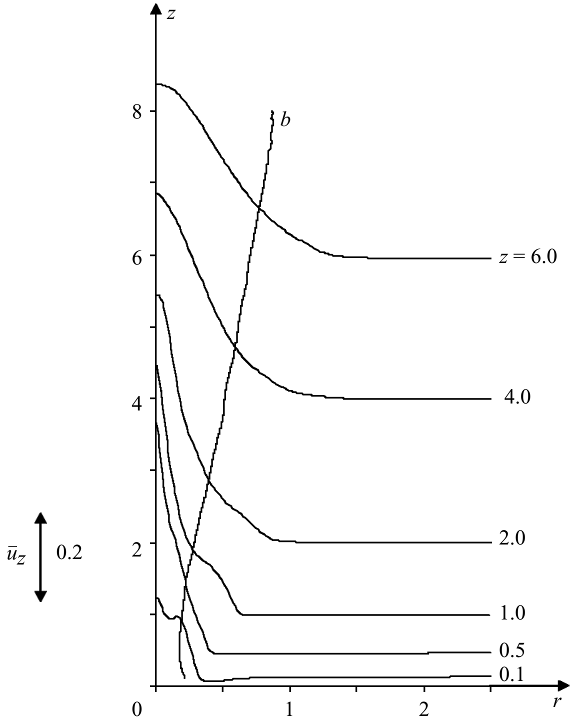

FIGURE 1. $\overline{u_z}$ radial profiles of mean vertical velocity component for several z and evolution of b plume radius, deduced from Gaussian fitting, with z.

centred on the geometrical plume axis. In addition, as we move away from the heat source, the velocity profiles are better approximated by a Gaussian distribution. It can be observed for $z = 0.1$ that the vertical velocity profile reveals the presence of a second off-axis maximum. Thus, the region very close to the heat source is subjected to an intense flow development, and self-similarity is not reached. The presence of such a second off-axis maxima has not been reported in the case of buoyant jets and consequently appears to be specific to pure plumes. The presence of the off-axis maxima will later be analysed in the context of unsteady flow development in the vicinity of the heat source.

Even though the velocity profiles close to the source are not perfectly fit by a Gaussian, in our case we obtain the best fit to the data of the form $u_{z,c}\exp(-r^2/b^2)$, where b provides a measure of the local radius of the plume. The vertical evolution of the plume width, b, is also shown in figure 1. It should be pointed out that the radial profiles of vertical velocity are displayed only at selected elevations, and much finer data were used to generate the plume width profile. Despite the approximation involved in the Gaussian fit, the vertical variation in b exhibits a necking phenomenon, i.e. the plume begins to contract immediately above the finite-sized heat source and at a finite elevation above the source, minimum plume radius is reached. Above such a position, the plume begins to enlarge with elevation. Note that the radius of the plume can also be estimated from thermal fields (not shown) and although not identical, the estimates from the velocity and temperature distributions were found to be relatively close.

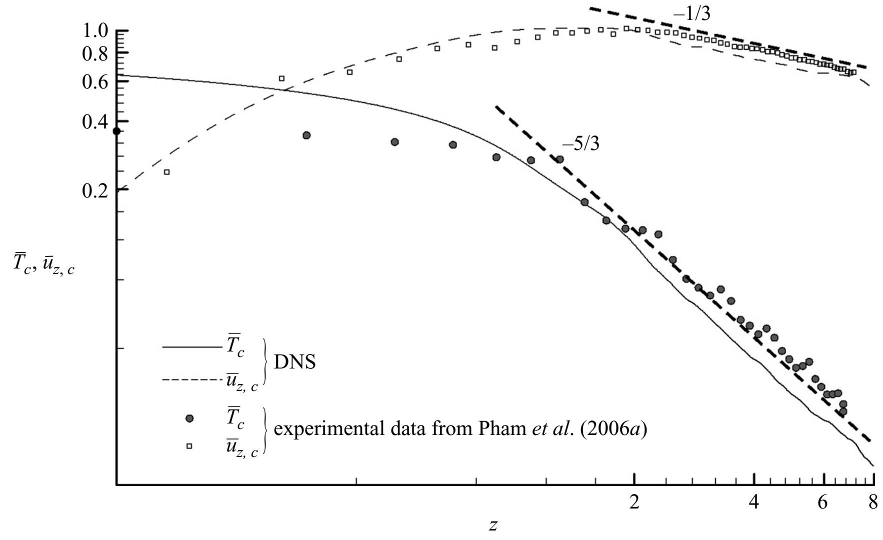

FIGURE 2. Change of mean velocity $\bar{u}_{z,c}$ and temperature $\bar{T}_c$ along the plume centreline.

The changes in velocity and temperature along the centreline are shown in figure 2. The vertical plume velocity along the plume axis begins to increase immediately above the source to reach a point of maximum velocity and above this point the plume decelerates while vertical velocity along the centreline monotonically decreases. In figure 2, experimental data extracted from Pham *et al.* (2006*a*) are likewise plotted. Numerical and experimental data show reasonable agreement both in magnitude and in the location of the maximum centreline velocity. A $-1/3$ power law can be observed away from the source as expected in theoretical prediction (Morton *et al.* 1956). Similar trends may be put forward for the change of temperature along the centreline. In the immediate vicinity of the heat source, numerical predictions are not as close to experimental data. According to Pham *et al.* (2006*a*), the heat source in their experiment was not flush mounted, which may have influenced the ascendant flow-field development.

The plume width as shown in figure 1 qualitatively resembles the theoretical result with a finite-sized source (Fannelop & Webber 2003). For quantitative comparison, we have redefined the plume width as $\tilde{b}(z) = \sqrt{q(q+\phi)/f}$, where q, f and ϕ are the mass, momentum and buoyancy fluxes. In figure 3 we plot $\tilde{b}(z)$ as a function of z/L, where the length scale is defined as $(\phi^2/g)^{1/5}$. The simulation results are compared with the theoretical prediction of Fannelop & Webber (2003) and experimental measurements of Liedtke & Schatzmann (1997). As expected, we observe the computed buoyancy flux to be conserved with height from the source. The computed mass and momentum fluxes were plotted on a $q^2\, vs.\, f^{5/2}$ plot (figure 3). As shown by Fannelop & Webber (2003), with the use of the Ricou & Spalding (1961) entrainment model, we find:

$$q^2 = q_o^2 + \left[\frac{8\alpha}{5g\phi}\right] f^{5/2}, \tag{4}$$

in which q_o and α correspond to mass flux at the source (here $q_o = 0$ for a pure thermal plume) and the entrainment coefficient, respectively. The theoretical linear relation between q^2 and $f^{5/2}$ is also plotted in figure 3 and although not perfect, the comparison is acceptable. The numerical data exhibit a nonlinear dependency

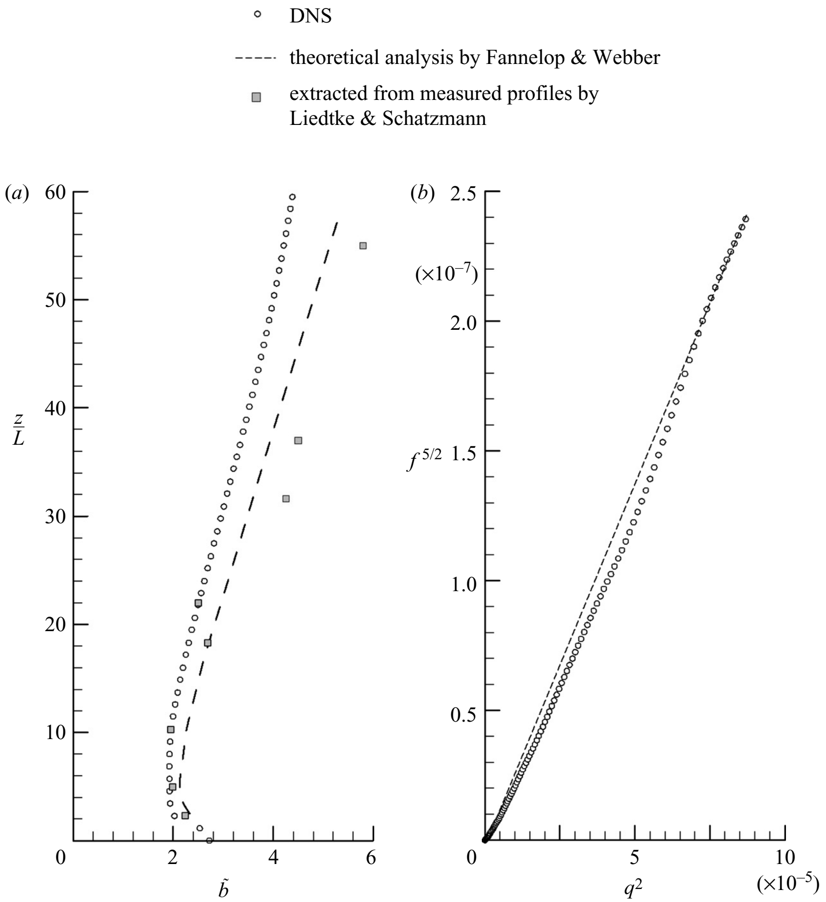

FIGURE 3. Numerical plume radius $\tilde{b}$ normalized by buoyant length scale $L=(\phi^2/g)^{1/5}$ evolution with regard to z/L and comparison with Fannelop & Webber theoretical model (line) and experimental results extracted from Liedtke & Schatzmann (1997). (*b*) $f^{5/2}\, vs.\, q^2$ extracted points from DNS and comparison with the analytical model from the Fannelop & Webber model.

of $q^2\, vs.\, f^{5/2}$ in the vicinity of the heat source. According to Fannelop & Webber (2003), comparison of data with theory should be done carefully, since analytical models are based mainly on arguments of self-similarity, which does not hold in the vicinity of a finite-sized heat source. Also, they show that different theoretical results are possible depending on the closure used for entrainment, and the self-similar power laws obtained with the Ricou & Spalding (1961) entrainment model is just one example among others.

3.2. *DNS assessment*

An overall idea of the general three-dimensional organization of the pure thermal plume can be gained from figure 4. The figure shows a three-dimensional isosurface of the vorticity magnitude. Also shown on the $x=-2.5$ (plane *a*) and $y=-2.5$ (plane *b*) planes are contours of the x and y components of vorticity, respectively. A concentration of vorticity may be observed at the bottom of the computational domain close to $z=0$, i.e. in the vicinity of the heat source. At the time shown, vortices

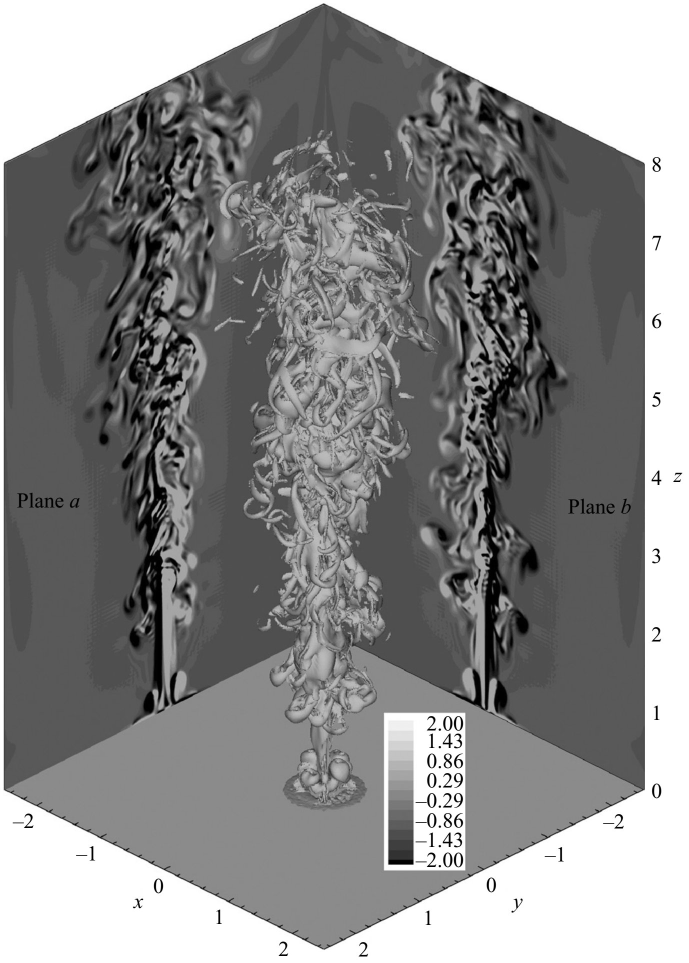

FIGURE 4. Instantaneous iso-vorticity modulus $\Omega = 3.0$ and distribution of the two components Ω_x, Ω_y in two planes at $x = 0$ (plane *a*) and $y = 0$ (plane *b*), respectively.

appear to be directly connected to the heated surface whereas for $0.5 \leqslant z \leqslant 1.0$, no structures are observed (unlike for $z > 1.0$). Note that vorticity magnitude gllows us to observe clearly the well-known classical regions of the plume, i.e. the laminar region, development of vortex roll-up and transition to turbulence beginning for $z > 1.0$, highlighted by increased vorticity concentration. In the far-field region ($z > 4.0$), a more complex topology is displayed and intense vortical regions are mainly organized as hairpin-shaped structures. These vortex structures principally populate in the high-shear region that surrounds the main ascendant flow field. The hairpin vortical structures clearly interlace with each other in a complex way as is typically the case in a turbulent flow (Chakraborty, Balachandar & Adrian 2005).

Through Lagrangian simulations, Soteriou, Dong & Cetegen (2002) investigated the near-field close to the source in order to underscore the unsteady dynamics of buoyant plumes. They suggest an unsteady mechanism with a pulsation frequency that is controlled by a Strouhal–Richardson number correlation, which implies that the underlying instability is inviscid in nature with a frequency equal to $\sqrt{g/w}$, where w is the nozzle width. Soteriou *et al.* (2002) describe the unsteady flow in the near field

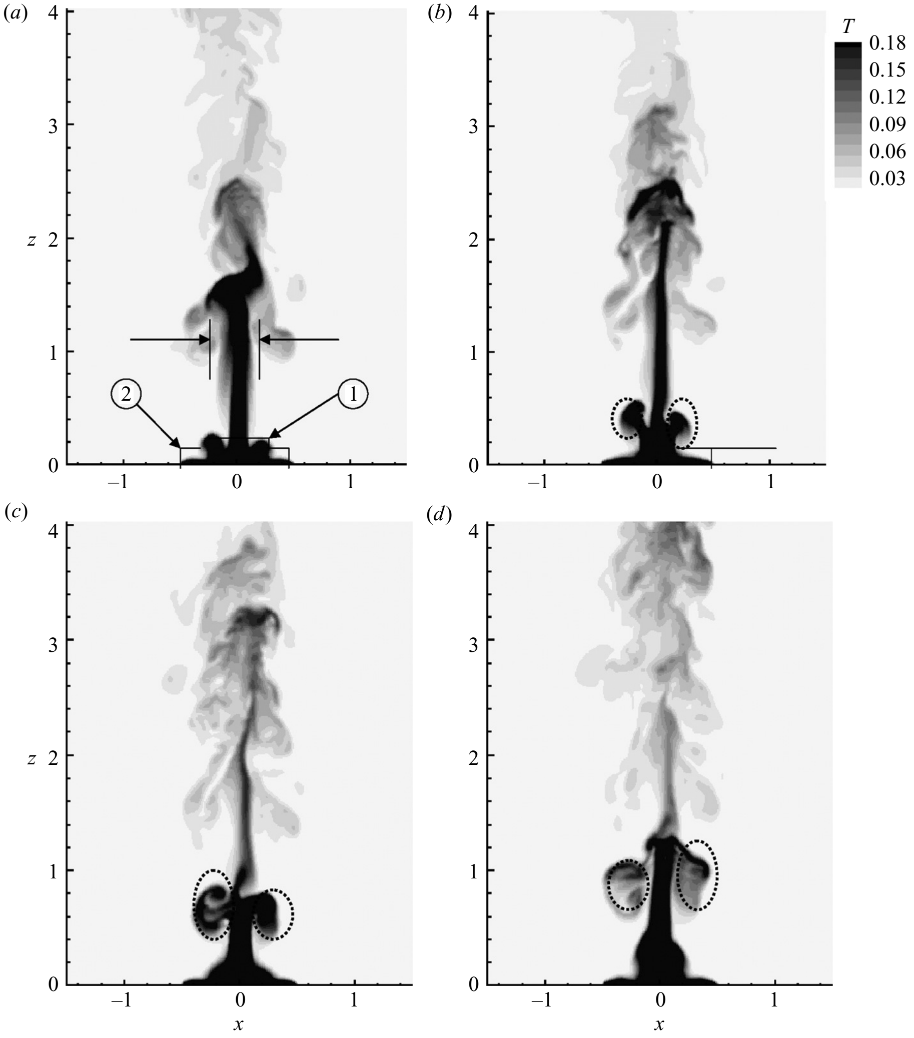

FIGURE 5. Distribution of temperature T in the region close to the heat source and its evolution over time. (*a*) $t = t_0$, (*b*) $t_0 + 1$, (*c*) $t_0 + 2$, (*d*) $t_0 + 3$.

of a buoyant jet as exhibiting different forms of behaviour ranging from symmetric shedding of a pair of line vortices to what appears to be asymmetric vortex shedding. They emphasize that such instabilities are dependent on the flow history and on the presence of perturbations. In addition, breakdown and vortex development generally occur in the vicinity of the nozzle outlet, i.e. in the near source field.

To emphasize how a pure thermal plume behaves in the near field of the heat source, figure 5 shows instantaneous contours of temperature on the vertical (x, z)-plane at four different times separated by unit non-dimensional time unit ($\Delta t = 1$). At $t = t_0$, a straight column of hot fluid is detected for $z \leqslant 1.6$, while just above this vertical location, temperature contours exhibit a different behaviour. An abrupt breakdown of the main column of hot fluid can be observed around $z \sim 1.6$ and the instability of the plume above this location results in enhanced mixing away from the plume axis. This behaviour can also be observed in the vorticity contours shown in figure 4 (especially in plane *a*) where the approximate axisymmetric columnar nature of the plume can be seen to exist close to the source, but rapidly breaks down into three-dimensional vortical structures. In figure 5 at $t = t_0$, incipient vortex roll-up very close to the heat source can be observed as the pair of hot blobs of fluid located on either side of the main column. These two structures observed on the (x, z)-plane are cut-sections of a single vortex ring that develops around the main ascending column of fluid. In the present case of a pure plume, buoyancy results in rapid upward acceleration of the fluid immediately above the heat source, forming the primary ascending column of fluid. The intense shear generated as the column ascends through the ambient surroundings undergoes instability and rolls into a vortex ring. As can be observed by $t = t_o + 1$, the vortex ring has moved up and is located at around $z = 0.3$. It still surrounds the main column of hot ascending fluid and the upward motion of the vortex ring is due to both self-induction and to buoyancy. At this time however, the main coherent vertical column of fluid extends until $z = 2.2$. At $t = t_0 + 2$ the newly formed vortex ring has convected up to a location $z = 0.6$ and the narrow column of hot fluid downstream from the vortex ring seems to have destabilized in the process of undergoing instability. By $t = t_0 + 3$, the top of the coherent central column of hot fluid extends up to $z = 1.2$, and the vortex ring, which has also moved up, lags somewhat behind and the scenario appears similar to $t = t_0$. It can be observed both in figure 5 and through a comparison of planes a and b in figure 4 that the vortex ring is not perfectly axisymmetric. From the incipient stages of formation, the vortex ring has strong three-dimensionality which can be observed in the vorticity iso-surface in figure 4. The three-dimensionality of the vortex ring grows with elevation and by $z \sim 2$ the vortex ring's interaction with the primary ascending core of hot fluid is sufficiently strong to render the column unstable as well. A time-dependent movie of the three-dimensional vortex structure (available with the online version of the paper) vividly illustrates this complex interaction process.

To clearly identify the nature of the instability arising from the heat source, figure 6 shows temperature as flooded contours overlaid on velocity vector plot on the (x, z)-plane passing through the axis in the immediate neighbourhood of the heat source ($z \leqslant 0.3$). Only the left-hand half of the plane is shown. In the region located close to the heat source, the dominant vertical motion occurs close to the axis for $x > -0.1$, while along the heat source (beginning at $x = -0.5$) a lateral flow lapping against the source is entrained because of the vertical fluid displacement. As can be observed at $t = t_0$ an incipient instability of the lapping flow along the bottom boundary is seen at around $x = -0.3$, where the velocity vectors are slightly displaced up and down, and a bump in the thermal field is observed. The instability grows over time to form a thermal plumelet, which is in fact a ring around the main column of ascending hot fluid. The plumelet is associated with a dominant counterclockwise (marked 1 in figure 6*d*) fluid motion on the outboard side and a weak clockwise vortex ring on the inboard. The plumelet is associated with a strong upward moving fluid motion, which at $t = t_0 + 3$ is comparable to fluid velocity in the main ascending column. By $t = t_0 + 4$, the plumelet and the associated vortex ring have moved up. The periodic instability of the lapping flow along the heat source results in the plumlet and the associated strong updraft is the source of the secondary peak observed in figure 1 for the vertical velocity profiles close to the heat source. Over time, the plumelet ring converges towards the axis and merges with the central column. In the process, the inboard vortex ring disappears and the remaining vortex ring on the outboard side of the plumlet survives and is seen in figure 4 as the vortex ring that surrounds the main ascending column of fluid.

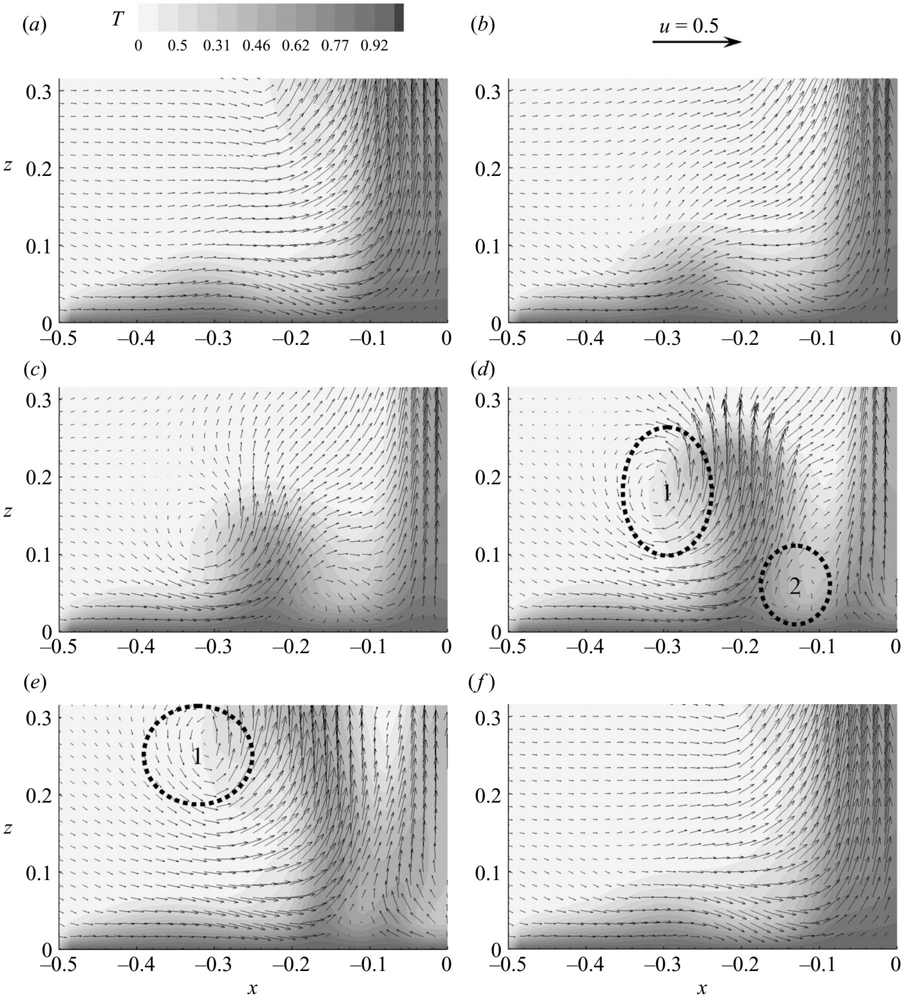

FIGURE 6. Visualization of instantaneous temperature T and velocity vector field in the vicinity of heat source and its change with regard to time. (*a*) $t = t_0$, (*b*) $t_0 + 1$, (*c*) $t_0 + 2$, (*d*) $t_0 + 3$, (*e*) $t_0 + 4$, (*f*) $t_0 + 5$.

Now we will focus on the transition from laminar to turbulent state in the plume. In general, transition is considered to be located when the fluctuating quantities (temperature and/or velocity component) reach a maximum along the centreline. In the fully turbulent regime, a constant level of fluctuation intensity is observed. The transition process and the location of fully developed turbulence can be expected to depend on the details of the heat source.Brahimi & Doan(1985) found that the shape of the heat source was important and strongly influenced the transition mechanisms. For instance, a hemispherical heat source will accelerate the transition process more quickly than in a pure thermal arising from a flat source. If we take into account all available data on transition, the fully turbulent region is generally observed to set from $3D^*$ to $5D^*$ above the heat source. Pham *et al.* (2005) performed an experimental investigation of a pure thermal plume arising from a flat heated disk and observed maximum fluctuation in thermal and velocity fields to occur close to $3.5D^*$. In order to ensure the adequacy of spatial and temporal resolution, we computed turbulent

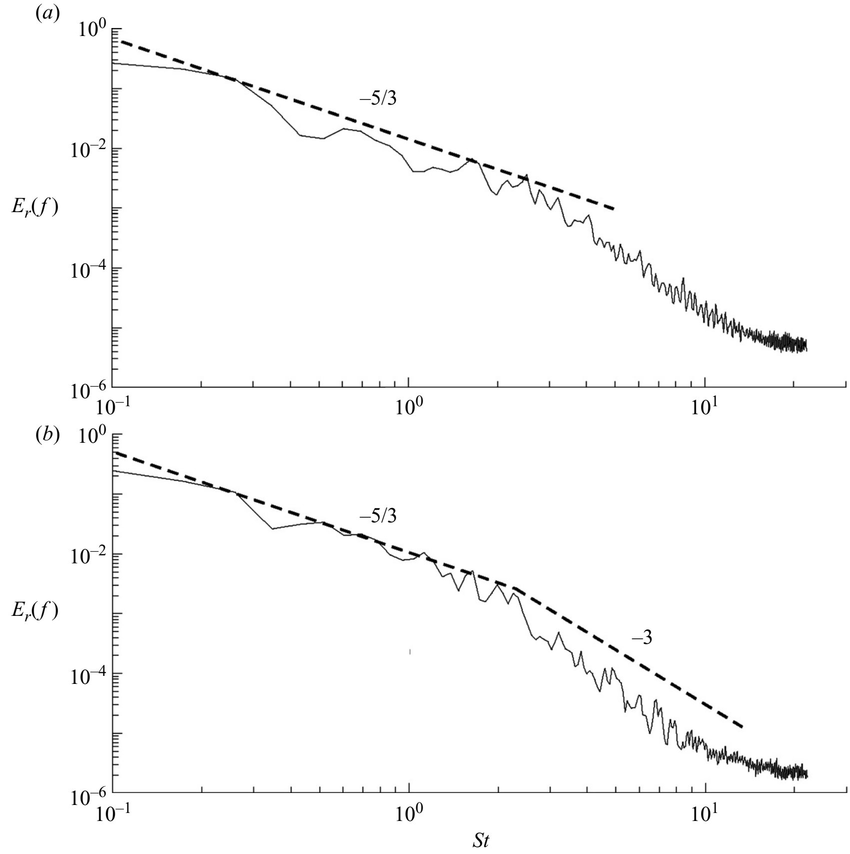

FIGURE 7. Temporal power spectrum of the temperature fluctuations $E_T(f)$ for two locations: (*a*) at plume axis ($x = 0$, $y = 0$, $z = 6$) and (*b*) outside plume boundary ($x = 0.5$, $y = 0$, $z = 6$).

dissipation, ε, and turbulent kinetic energy, $\overline{u_i' u_i'}$, from which the Kolmogorov length scale, η, Kolmogorov time scale, τ, were computed at several different points and the smallest Kolmogorov scales were compared with the physical mesh size and computational time step. The ratio between physical mesh size and Kolmogorov scale was observed to be about 1.02, and therefore the mesh size was considered fine enough to capture the entire range of flow scales (Kim, Moin & Moser 1987; Moin & Mahesh 1998). A second test, which is specific to buoyant plumes, consists in analysing temperature fluctuations and their spectral energy distributions with regard to the radial position. Energy distributions were plotted against non-dimensional frequency, $St = f^* D^* / U_0^*$. On the plume axis at $z = 6$ (figure 7*a*), the power spectra of temperature fluctuations shows the expected $-5/3$ Kolmogorov power law. Away from the axial location, at a radial location close to the outer edge of the plume boundary ($x = 0.5$, $y = 0$, $z = 6$), a similar trend is observed in the spectral distribution of thermal fluctuation (figure 7*b*). The inertial–convective regime with the $-5/3$ decay is still present, but is immediately followed by a greater decay of -3 power law. This is a specific feature of buoyant jet flows and it characterizes the inertial–diffusive subrange (List 1982; Kotsovinos 1991; Noto, Teramoto & Nakajima 1999). Buoyancy strongly affects the turbulence production, distribution and dissipation mechanisms

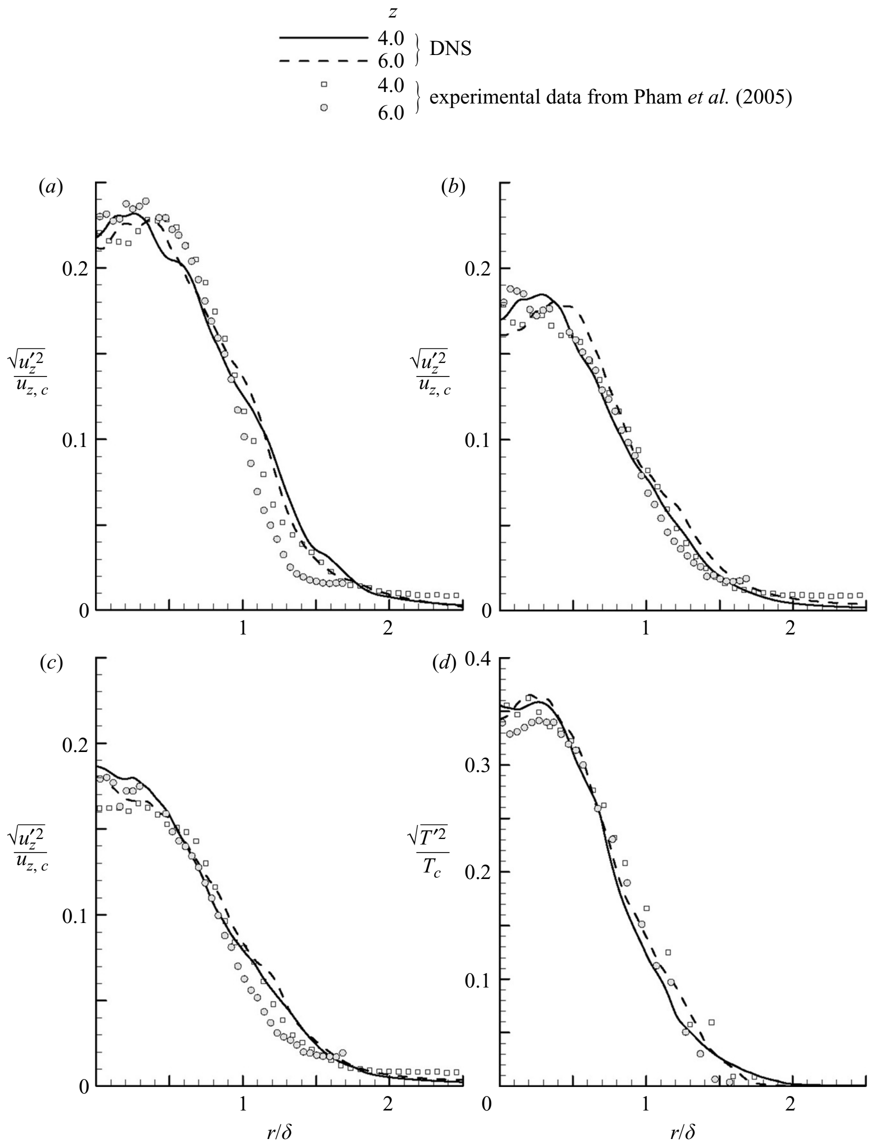

FIGURE 8. Non-dimensional turbulent intensity of (*a*) axial, (*b*) radial and (*c*) circumferential velocity component and (*d*) temperature profiles for two locations in the turbulent region.

so that the jump from the −5/3 to −3 subrange corresponds to a stronger energy feeding owing to the large plume vortices, which are driven by the buoyancy force.

In the turbulent region, decay of centreline mean temperature and vertical velocity components (shown in figure 2) were found to follow the −1/3 and −5/3 power laws predicted by self-similar theories. Figure 8 presents normalized root-mean square profiles of vertical, radial and circumferential velocity components as well as temperature for two different vertical locations. The results shown are both time and circumferentially averaged and are normalized by the mean centreline vertical velocity, $\overline{u}_{z,c}$, (the subscript c corresponds to the plume centreline). Radial distances were normalized by the momentum length scale, $\delta(z)$, which will be defined later in

(8). The corresponding experimental data extracted from Pham *et al.* (2005) were likewise plotted in the figure. The radial and circumferential turbulent intensities are similar, while the axial velocity fluctuations are about 30 % larger. George *et al.* (1977) experimentally studied a buoyant jet and put forward the hypothesis that the peak turbulent intensities were located off-axis. Both the computational and the experimental results exhibit this behaviour. The amplitudes of radial, circumferential and axial fluctuation levels reported in the literature are generally in the 15 to 30 % range and the present results are well within that. Temperature fluctuation profiles reveal a slight off-axis peak of about 36 %, whereas in the literature slightly higher thermal fluctuation levels of about 40 % and 42 % were reported by George *et al.* (1977) and Papanicolou & List (1988). Temperature fluctuations are always found to be greater than the velocity fluctuations and, as reported by Agator & Doan (1982), turbulence intensities are linked to overall plume development and heat source geometry. The configuration of the heat source in the present simulations is identical to those used in the experiments of Pham *et al.* (2005), thus resulting in satisfactory agreement.

3.3. *Pulsating mechanism*

Interaction between the ascending hot fluid and its surroundings is essential to the development of the plume. When plumes or buoyant jets arise in an otherwise quiescent environment, the ascendant column of fluid is separated from the stationary ambient fluid by a region of strong shear. The vortex sheet develops in an unstable way and rolls up into a sequence of discrete vortex rings. Such vortices interact by rolling around each other and as they do so, they engulf irrotational ambient fluid and incorporate it into the turbulent ascending flow. Thus, these vortices play a key and direct role in the entrainment mechanism. Sreenivas & Prasad (2000) analysed a pure plume and showed that as the potential energy stored in unstable stratification is released, plumes can entrain more than jets. According to Dimotakis (1986), the entrainment process may be divided into steps. First, in the induction phase, ambient fluid is inducted into the ascending turbulent fluid. Turbulent straining of the inducted fluid then reduces its spatial scale to a small value at which viscous diffusion dominates. The inducted fluid then mixes at the molecular level with the turbulent flow. Sreenivas & Prasad (2000) emphasize that the key mechanism in the entrainment process is induction-based and that mixing at the larger scales controls plume development. The entrainment process is sensitive to the development of large scales and their unsteady dynamics. For example, spatial development of pure thermal turbulent plumes was analysed under a rotating condition for the heat source by Pham *et al.* (2006*b*). Close to the source, the Coriolis effect strongly alters the plume shape, and significantly increases entrainment; but above a threshold elevation, the thermal plume virtually forgets the rotation effect and behaves as would a regular thermal plume. Similar sensitivity in entrainment prediction was observed in the coalescence of two turbulent plumes modelled by Kaye & Linden (2003).

In order to extract large-scale coherent structures from the turbulent flow field, we first define a length scale based on a two-point correlation. We have computed the two-point correlation of vertical velocity along the plume centreline as follows:

$$R_{11}(z, \mathrm{d}z) = \frac{\overline{u'_z(z)u'_z(z+\mathrm{d}z)}}{\sqrt{\overline{u'^2_z(z)}}\sqrt{\overline{u'^2_z(z+\mathrm{d}z)}}} \tag{5}$$

in which subscript 1 designates the vertical velocity component and dz corresponds to the vertical distance between the two points along the plume axis. The integral

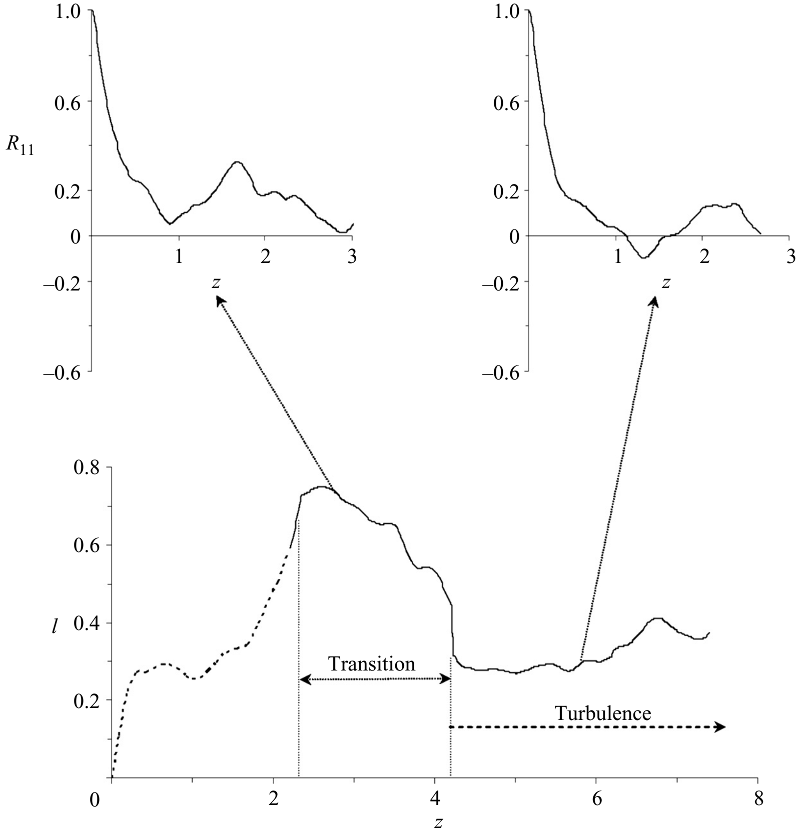

FIGURE 9. Spatial correlation coefficients R_{11} of vertical velocity at two different positions on the plume axis in transition and turbulent region and evolution of integral length scale l with regard to z along the plume axis.

length scale is subsequently defined based on the two-point correlation as:

$$l = \int_0^{\infty} R_{11}(z, \mathrm{d}l)\, \mathrm{d}l. \tag{6}$$

The integral length scale was computed all along the vertical plume axis and its change with z is shown in figure 9. Also shown in the figure are two-point correlations at two different elevations from the heat source. Three different zones can be identified. In the region close to the heat source dominated by the periodic puffing of vortical structures ($z \leqslant 2.5$) the spatial correlation rapidly decays so that l remains small. This region corresponds to development of the ascendant fluid motion, and large structures at the periphery of the main ascendant current evolve under strong acceleration. As a consequence, vortical structures rapidly evolve and merge with the main stream, as shown in figure 6, and spatial correlations rapidly decorrelate. In the transition region ($2.5 \leqslant z \leqslant 4.0$), structures are somewhat altered during their upward convection, but they retain sufficient integrity to maintain a higher level of spatial correlation. In the fully turbulent region ($z \geqslant 4.0$) the coherent vortical structures undergo rapid evolution and break down to finer-scale structures leading to a reduction in the correlation length scale. In the fully turbulent region, the integral scale of correlation remains almost constantly close to $l \sim 0.35$. In the transitional region, a second peak is observed in the two-point correlation at a vertical separation of $dz = 1.75$, which corresponds to the spacing between the adjacent coherent structures. In the turbulent region, the correlation decays to zero faster, but a second peak is still observed at a larger vertical separation of $dz = 2.2$. The interpretation is that the vestiges of the periodic large-scale coherent vortex rings are still present in the turbulent regime, but the small-scale turbulent correlation decays faster.

In this part of our study, we have been focusing on the dynamics of the large-scale coherent structures. As illustrated in figure 4, straightforward visualization of the present highly resolved simulation will result in a complex vortical structure that highlights the wide range of length scales present. We will apply a low-pass filter to the data in order to extract only the large-scale vortical structures. To do so, a Gaussian filter is defined as:

$$G_{\overline{\Delta}}(x) = \sqrt{\frac{6}{\pi \overline{\Delta}^2}} \exp(-6x^2/\overline{\Delta}^2) \tag{7}$$

with $\overline{\Delta}$ the filter width. As in large-eddy simulation methodology $G_{\overline{\Delta}}(x)$ was applied to direct numerical results in order to separate the large-scale motion. It should be emphasized that the simulations resolved all the length scales and that the spatial filter was applied only *a posteriori*. Other spatial filters such as a box or a top-hat filter (Meneveau & Katz 2000; da Silva & Métais 2002) may likewise be applied. Here we have chosen a Gaussian filter, since other filters were observed to yield similar results. Irrespective of the filter employed, the width of the filter, $\overline{\Delta}$, is the critical parameter controlling the extracted large-scale structures. Given that the filtering procedure is designed to extract coherent structure and to assess its dynamics, we have chosen the filter width based on a two-point correlation length scale such as $l = \overline{\Delta} = 0.35$. Thus, large-scale turbulent motions are defined to be those larger than the correlation length scale, while those smaller are deemed subscale.

Here we use the swirling strength, λ_{ci}, defined as the imaginary part of the complex conjugate eigenvalues of the local velocity gradient tensor, to extract the vortical structure from the filtered large-scale flow field (Zhou *et al.* 1999; Chakraborty *et al.* 2005). If at any given point the velocity gradient tensor has all three real eigenvalues, then locally the flow is not swirling and λ_{ci} is set to zero. First, in order to shed light on the flow complexity, the swirling strength was computed on both the raw and filtered data and figure 10 reveals an isosurface contour of λ_{ci}^2 that corresponds to 40 % of the maximal value in the turbulent region ($4.0 \leqslant z \leqslant 6.0$). A wide range of length scales and hairpin-like vortical structures surrounding ascendant plume motion can be observed in the computed flow. Even though the filtering process has eliminated small-scale structures, the extracted large-scale structures look complex and their dynamics can be expected to be non-trivial. To highlight the induced fluid motion, the instantaneous velocity vectors are plotted on two different (x, y)-planes at $z = 5.0$ and 5.7, i.e. at locations, respectively, below and above the rolled-up structure designated as ‘1’ in figure 10(*b*). The vector plots clearly reveal the clockwise and counterclockwise circulating regions, which indicate the spiralling nature of the plume (Cortese & Balachandar 1993). Stagnation points are located close to the plume boundary and correspond to cold fluid flowing in from the environment process and spreading horizontally. However, at $z = 5.0$, most of the velocity vectors are inward-oriented whereas at $z = 5.7$, most of the velocity vectors are outward-oriented with regard to the plume axis. Such instantaneous velocity behaviours are intimately linked to the hairpin-like vortex presence. During its convection and rotation, the

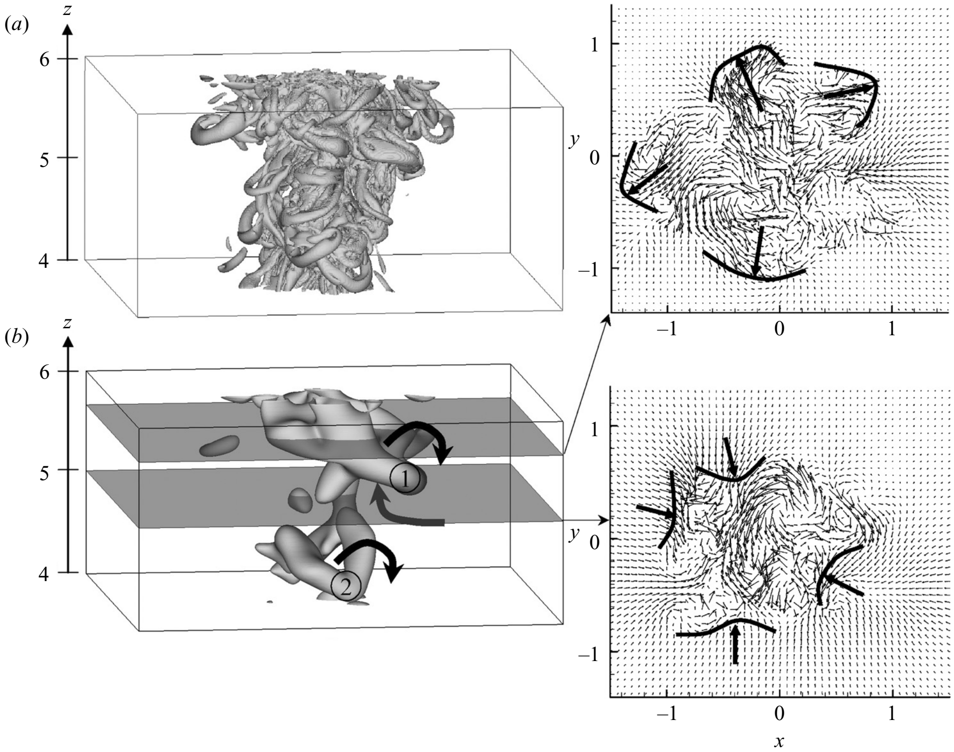

FIGURE 10. Iso-surface of λ_{ci}^2 for the large structures for raw and filtered data and distribution of velocity field on two horizontal planes; under and upper structure ‘1’, respectively: (a) at $(z = 5.0)$ and (b) at $(z = 5.7)$.

vortex rings have a tendency to entrain fluid at the bottom and eject fluid out of the plume at the top of the structure. Thus, expansion of a pure thermal plume occurs in terms of instantaneous lateral exchange between the ascendant flow and its vicinity, driven by time-dependent expulsion and ingestion of fluid by the vortical structures. Such mechanisms were discussed by Basu & Narasimha (1999) in their study of reduction of entrainment by addition of buoyancy away from the source by volumetric heating. We may expect additional buoyancy in a plume to provide local acceleration of ascendant flow, which in turn should favour entrainment. However, as clearly observed by Sreenivas & Prasad (2000), addition of off-source buoyancy entails a decrease of the resulting angular velocity, i.e. an increase of the turnover time resulting in a decrease of entrainment.

In order to appreciate better the relation between coherent vortical structures and entrainment, it is necessary to define a local instantaneous entrainment coefficient. The capacity of buoyant plumes and jets to attract quiescent fluid from their immediate surroundings has traditionally been deduced from averaged fields and the entrainment coefficient on an average basis is defined as the ratio between mean inward radial velocity outside the plume and mean vertical velocity on the axis. Such a definition is naturally convenient from an experimental point of view, since the radial and vertical mass flow rate fluctuations are averaged out. Dibble *et al.* (1987) estimated the contribution of fluctuating terms to mass flux integral to be equal to approximately 20 % of the whole mass flow rate. To estimate entrained fluxes precisely, a direct measurement method is required along the lines of that of Ricou & Spalding (1961). They measured the entrainment flux of a turbulent jet by surrounding the jet with a porous-walled cylindrical chamber equipped to measure pressure drop, which was expected to be directly proportional to entrained mass flow rate. However, it is not clear whether such an experimental set-up will guarantee accurate measurements, and not rather tend to worsen flow-field integrity. Pham *et al.* (2005) performed direct entrainment measurements in turbulent pure plume through instantaneous three-dimensional velocity measurements. The method consists in measuring, as accurately as possible, the velocity component in the plume periphery, i.e. regions where ambient fluid is engulfed into the ascendant column. It is non-trivial to define the border between the ascendant flow field and its surroundings. The length scale, b, as defined by Fannelop & Webber (2003) corresponds to the distance from the axis at which velocity amplitude is $1/e$ of that on the axis. At that location, flow field is still mainly vertically oriented and is therefore not an ideal location for estimating mass flow rate exchange between the plume and its immediate surroundings. To locate the plume border, Pham *et al.* (2005) defined a momentum balance length scale, $\delta(z)$, as:

$$\delta^2(z) = \frac{2\left(\displaystyle\int_0^\infty \bar{u}_z r \,\mathrm{d}r\right)^2}{\displaystyle\int_0^\infty \bar{u}_z^2 r \,\mathrm{d}r}. \tag{8}$$

While the vertical variation of $\delta(z)$ follows that of $b(z)$, it is observed to be sufficiently far away from the axis to study mass flow exchange between ascendant motion and its environment. In addition, it is worth noting that the radial velocity component decays as a function of $1/r$ by continuity. So, the precise location of the border does not directly interfere with the accuracy of the entrainment mass flow rate estimation since ru_r remains at a constant level. Based on such arguments, the instantaneous entrainment coefficient is defined as:

$$\alpha(t, z) = \frac{m(t, z)}{\rho_\infty \overline{\overline{u_z(z)}}}, \tag{9}$$

in which $m(t, z)$ corresponds to the instantaneous mass flux rate per unit surface area, integrated around the circumference of the ascendant flow field. It is also important to underline that when dealing with instantaneous data, fluid may enter into the plume as well as being ejected from it.

To explore the entrainment mechanism as the turbulent coherent structures advect and deform, figure 11 shows the isosurface of λ_{ci}^2 equal to 40 % of the maximum value at four different time instances. Also plotted on the side are vertical profiles of instantaneous entrainment coefficient at these time instances. Wide variations in the instantaneous entrainment coefficient are detected. For instance, at $t = t_0$, α reaches a peak level of 0.23 just under the large structure identified in the turbulent plume and denoted in the figure as ‘1’. Away from the peak, both above and below, low levels of α close to 0.04 are detected and these minimum locations coincide with spatial locations that are to be found just above the vortical structures. As soon as new coherent structures advect into position (such as that designated by ‘2’ in figure 11), a local increase of α is realized. Following the structure–entrainment rate evolution with time, the vertical evolution of structures ‘1’ and ‘2’ is tracked by spatial evolution of the α peak. Furthermore, at $t = t_0 + 2$, structure ‘2’ is subjected to a vertical stretching effect; and as a consequence it spatially enlarges the corresponding α peak.

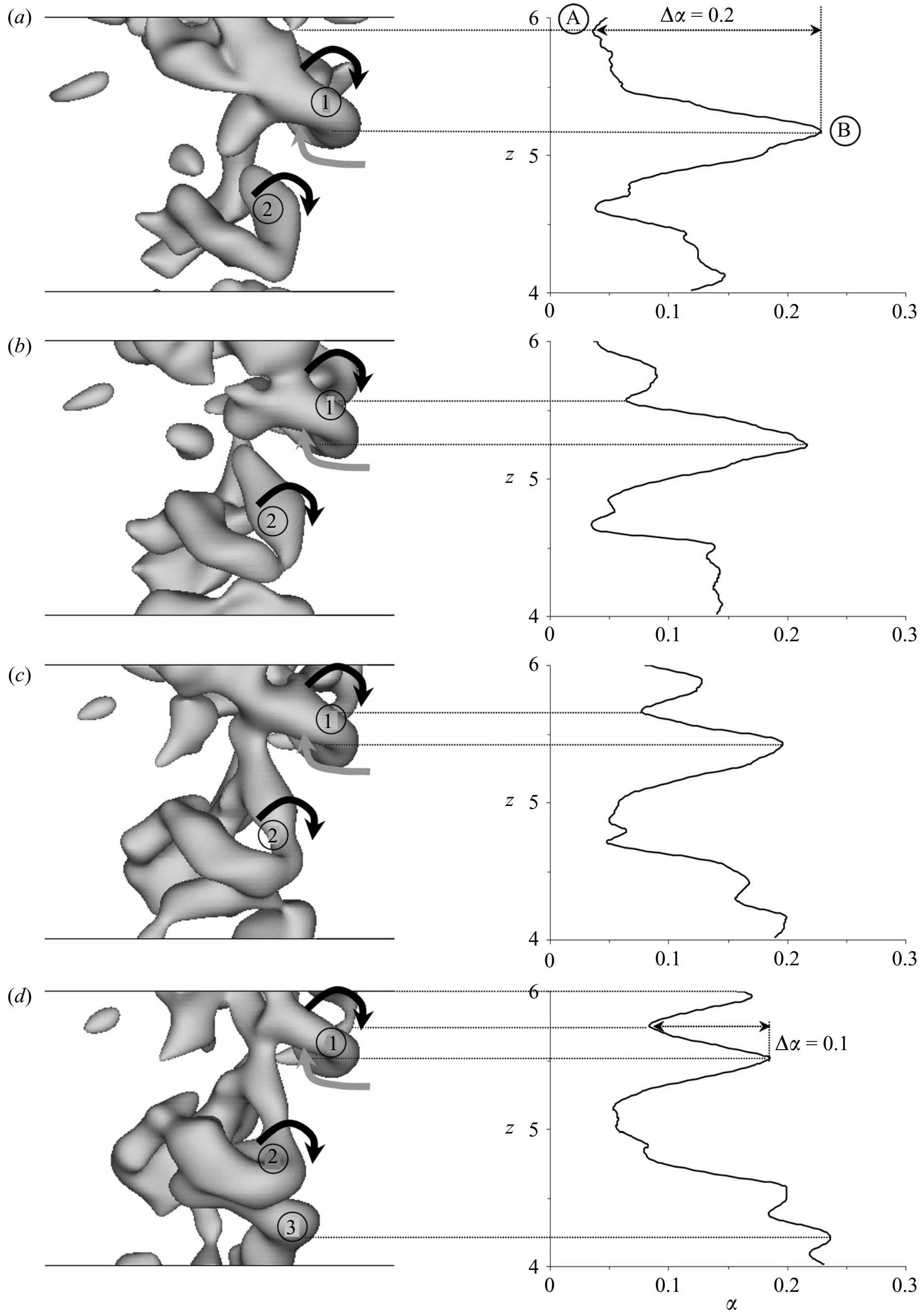

FIGURE 11. Visualization of large structures using λ_{ci}^2 for several times and its correlation with the instantaneous entrainment coefficient α. (*a*) $t = t_0$, (*b*) $t_0 + 1$, (*c*) $t_0 + 2$, (*d*) $t_0 + 3$.

Sreenivas & Prasad (2000) advanced a vortex dynamic balance model for entrainment in jets or plumes, where entrainment depends on overall circulation, which increases only marginally. However, as seen in the figure, it is the local instantaneous evolution of coherent structures that literally drives the dominant entrainment process. It has

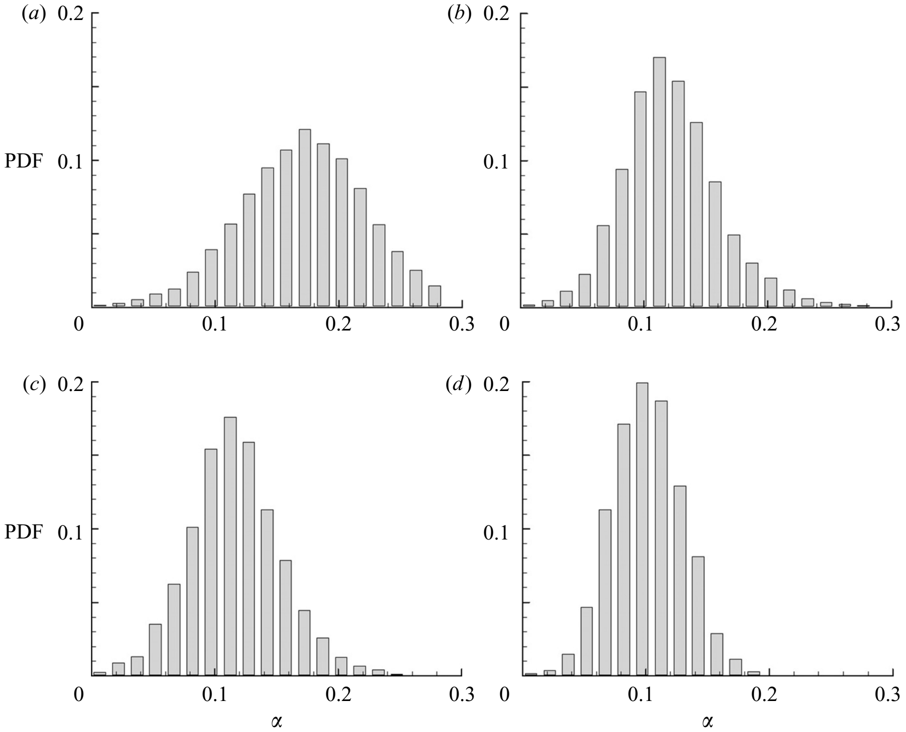

FIGURE 12. Statistical distributions of entrainment coefficient for several vertical positions in the z-direction. (*a*) $z = 1$, (*b*) 2, (*c*) 3, (*d*) 4.

been clearly observed in planes perpendicular to the plume axis that the in-plane velocities are mainly inward-oriented, highlighting local and intermittent engulfment of ambient fluid at the bottom of the coherent vortical structures. On the contrary, expulsion of plume fluid occurs just above structures. Plume evolution is mainly driven by these two different steps, i.e. expulsion and contraction mechanisms. The minimum of entrainment arises during the expulsion phase, while the plume entrains a maximum amount of ambient fluid during the contraction phase. These two mechanisms actually correspond to the pulsating behaviour that is often described in buoyant jets or plumes. For example, the pulsating mechanism in a turbulent plume was reported in experiments with instantaneous three-dimensional velocity measurements (Pham *et al.* 2005). The present DNS results allow us to further quantitatively depict this entrainment–coherent structure interaction.

As entrainment is closely linked to vortex dynamics along the plume periphery, it is expected that wide α variation will occur over time. Entrainment mechanisms and the proper estimation of the entrainment coefficient have been studied actively. The value of α classically ranges from 0.08 and 0.12 in the literature. As shown in figure 11, instantaneous α may reach levels almost three times higher than the average level. Statistics of the instantaneous entrainment coefficient were studied and their distributions have been plotted for several z locations (figure 12). Close to the heat source ($z = 1.0$), the distribution is very wide and is centred approximately around 0.16. As discussed above, the region close to the heat source is mainly driven by the puffing phenomenon, i.e. large eddies are generated and behave as connected vortex rings around the main ascendant current. In addition, the inward motion of fluid

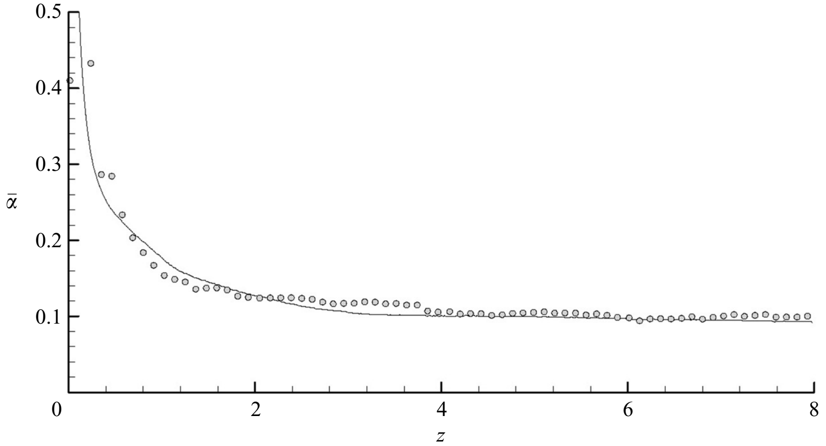

FIGURE 13. Variation of average entrainment coefficient with regard to vertical position obtained from —, DNS simulation and ○, experimental results using the direct method (Pham *et al.* 2005).

driven by continuity to balance the ascendant motion contributes to the entrainment of the plume close to the bottom. At higher vertical positions, $z = 2.0$ and to a lesser extent $z = 4.0$, distribution of α levels is more and more centred around a value close to 0.12 and fluctuations around this level weaken. In the fully turbulent area ($z = 6.0$), the distribution of entrainment coefficient peaks at around 0.1, and is narrower. The distributions of entrainment coefficient at other elevations in the fully turbulent regime are similar. From such a distribution, an average entrainment coefficient, $\bar{\alpha}$, was computed and shown in figure 13 as a function of elevation. Also plotted in the figure are average entrainment coefficients obtained in the experiments of Pham *et al.* (2005). Good agreement between experimental and DNS results can be observed over the entire elevation, including the region close to the heat source.

4. Conclusion

We examine the development of a thermal plume originating from a localized heat source using direct numerical simulation. The Reynolds number of the plume, based on source diameter and the characteristic buoyancy velocity, is chosen to be 7700, which is sufficiently large that the flow transitions to a fully turbulent state. The corresponding maximum Grashof number, based on the height of the computational domain, is 2.2×10^{10}. A highly resolved grid of 622 million points is used and *a posteriori* tests confirm that the grid resolution is fine enough to resolve fully all turbulent scales in the plume down to the Kolmogorov scale.

We pay close attention to the flow field in the vicinity of the heat source and in this region numerical simulation exhibits features that are specific to thermal plumes arising from a finite-sized source. In particular, we observe the plume to form a neck, which corresponds to a minimum plume cross-section and a maximum vertical velocity. Following Fannelop & Webber (2003), we compare the numerical simulation results with analytical models. Here, at the source, only heat is added with no mass or momentum addition and accordingly sufficiently for away from the source, the vertical evolution of the mass, momentum and buoyancy fluxes computed from the simulation are in good agreement with the theoretical linear relation between q^2 and $f^{5/2}$ predicted for a pure thermal plume (here q and f are the mass and momentum fluxes). However, close to the source, the numerical data exhibit a nonlinear dependency of q^2 on $f^{5/2}$. The difference signifies a departure from the self-similar behaviour in the case of a finite-sized heat source.

Investigation of the time-dependent flow behaviour in the vicinity of the source illustrates a puffing phenomenon. The behaviour arises from the periodic development of vortical structures close to the source. Such structures literally lean up against the heat source before being propelled in a vertical direction. This process is driven by periodic roll-up of the interfacial shear between the ascending column of fluid and the ambient surroundings into coherent vortex rings. The near-source region is then characterized mainly by non-stationary convection of vertical structures, which are highly three-dimensional even as they form close to the heat source. The vortex ring ascends with the plume and at a non-dimensional elevation of about $z \sim 2$ it strongly interacts and destabilizes the central column of ascending fluid and a complex turbulent flow subsequently arises. In the transitional region, a second peak is observed in the two-point correlation at a vertical separation of $\mathrm{d}z = 1.75$, which corresponds to the spacing between the adjacent coherent structures. In the turbulent region, the correlation decays to zero faster, but a second peak is still observed at a larger vertical separation of $\mathrm{d}z = 2.2$. The interpretation is that the vestiges of the periodic large-scale coherent vortex rings are still present in the turbulent regime, but the small-scale turbulent correlation decays faster.

In order to capture the dynamics of the large-scale coherent structures, we first apply a low-pass Gaussian spatial filter to the DNS data. The specific filter width was chosen equal to the integral length scale of the two-point correlation in the fully developed turbulent region. The vortical coherent structures were identified by plotting the isosurface of the imaginary part of the complex eigenvalue of the velocity gradient tensor. By simultaneously presenting the large-scale vortical structures and the local instantaneous entrainment, we establish a direct link between the two. Above the spatial location of the coherent structures, it is observed that a contraction mechanism emerges and underscores spatially localized and instantaneous entrainment. Below the structure, an expulsion mechanism ejects fluid from the core of the plume. From data obtained, we have demonstrated that such instantaneous mechanisms drive the entrainment process and that the instantaneous entrainment coefficient shows large variation in both time and space with local values up to three times higher than the average entrainment level. It is the net balance which provides the actual mean entrainment aptitude of the plumes, and the mean entrainment coefficient computed from the DNS data is in agreement with recent experimental measurements.

Computations were carried out at the Institut de Développement et des Ressources en Informatique Scientifique (IDRIS), the computational centre of the Centre National de la Recherche Scientifique (CNRS). The authors wish to warmly thank the head of IDRIS department, V. Alessandrini, for his unstinting support.

REFERENCES

Agator, J. M. & Doan, K. S. 1982 Turbulence structure of axisymmetric thermal plumes. *Mech. Res. Commun.* **9**, 159–164.

Bastiaans, R. J. M., Rindt, C. C. M., Nieuwstadt, F. T. M. & Van Steenhoven, A. A. 2000 Direct and large-eddy simulation of the transition of two- and three-dimensional plane plumes in a confined enclose. *Intl J. Heat Mass Transfer* **43**, 2375–2393.

Basu, A. J. & Narasimha, R. 1999 Direct numerical simulation of turbulent flows with cloud-like off-source heating. *J. Fluid Mech.* **385**, 199–228.

Bill, R. R. & Gebhart, B. 1975 The transition of plane plumes. *Intl J. heat Mass Transfer* **18**, 513–526.

Billeter, L. & Fannelop, T. K. 1989 Gas concentration over an underwater gas release. *Atmos. Environ.* **23**, 1683–1694.

Bhat, G. S. & Narasimha, R. 1996 Volumetrically heated jet: large eddy structure and entrainment characteristics. *J. Fluid Mech.* **329**, 303–330.

Brahimi, M. & Doan, K. S. 1985 Interaction between two turbulent plumes in close proximity. *Mech. Res. Commun.* **12**, 149–155.

Cantero, M. I., Balachandar, S., Garcia, M. H. & Ferry, J. P. 2006 Direct numerical simulations of planar and cylindrical density currents. *J. Appl. Mech.* **73**, 923–930.

Cantero, M. I., Lee, J. R., Balachandar, S. & Garcia, M. H. 2007 On the front velocity of gravity currents. *J. Fluid Mech.* **586**, 1–39.

Chakraborty, P., Balachandar, S. & Adrian, R. J. 2005 On the relationships between local vortex identification schemes. *J. Fluid Mech.* **535**, 189–214.

Cook, A. W. & Riley, J. J. 1996 Direct numerical simulation of a turbulent reactive plume on a parallel computer. *J. Comput. Phys.* **129** , 263–283.

Cortese, T. & Balachandar, S. 1993 Vortical nature of thermal plumes in turbulent convection. *Phys. Fluids* A **5**, 3226–3232.

Desrayaud, G. & Lauriat, G. 1993 Unsteady unconfined buoyant plumes. *J. Fluid Mech.* **252**, 617–646.

Dibble, R. W., Schefer, R. W., Chen, J. Y. & Hartmann, V. 1987 Velocity and density measurements in a turbulent nonpremixed flame with comparison to numerical model predictions. *Sandia Rep. SAND85-8233.* UC-304.

Dimotakis, P. E. 1986 Two-dimensional shear-layer entrainment. *AIAA J.* **24**, 1791–1796.

Fannelop, T. K. & Webber, D. M. 2003 On buoyant plumes rising from area sources in a calm environment. *J. Fluid Mech.* **497**, 319–334.

George, W. K., Alpert, R. L. & Tamanini, F. 1977 Turbulence measurements in an axisymmetric experiment on a round turbulent buoyant plume. *Intl J. Heat Mass Transfer* **20**, 1145–1154.

Hunt, G. R. & Kaye, N. G. 2000 Virtual origin correction for lazy turbulent plumes. *J. Fluid Mech.* **435**, 377–396.

Hunt, J. C. R., Wray, A. A. A. & Moin, P. 1988 Eddies; stream and convergence zones in turbulent flows. *Proc. Summer Program of the Centre for Turbulence Research, NASA Ames/Stanford University*, pp. 193–207.

Kaye, N. B. & Linden, P. F. 2003 Coalescing axisymmetric turbulent plumes of vortex. *J. Fluid Mech.* **502**, 41–63.

Kim, J., Moin, P. & Moser, R. D. 1987 Turbulent statistics in fully developed channel flow at low Reynolds number. *J. Fluid Mech.* **177**, 133–166.

Lessani, B. & Papalexandris, M. V. 2006 Time-accurate calculation of variable density flows with strong temperature gradients and combustion. *J. Comput. Phys.* **212**, 218–246.

Liedtke, J. & Schatzmann, M. 1997 Dispersion from strongly buoyant sources. *Final Rep. EU-Project* EV5V-CT-93-0262. University of Hamburg, Meteorological Institute.

List, E. J. 1982 Turbulent jets and plumes. *Annu. Rev. Fluid Mech.* **14**, 189–212.

Kotsovinos, N. E. 1991 Turbulence spectra in free convection flow. *Phys. Fluids* **3**, 163–167.

Majda, A. & Sethian, J. 1985 The derivation and numerical solution of the equations for zero mach number combustion. *Combust. Sci. Technol.* **42**, 185–205.

Meneveau, C. & Katz, J. 2000 Scale invariance and turbulence models for large-eddy simulation. *Annu. Rev. Fluid Mech.* **32**, 1–32.

Moin, P. & Mahesh, K. 1998 Direct numerical simulation: a tool in turbulence research. *Annu. Rev. Fluid Mech.* **30**, 539–578.

Morton, B. R., Taylor, G. I. & Turner, J. S. 1956 Turbulent gravitational convection from maintained and instantaneous sources. *Proc. R. Soc. Lond.* A **234**, 1–23.

Nakagomeka, H. & Hirata, K. 1976 The structure of turbulent diffusion in an axi-symmetrical thermal plume. *Proc. ICHMT Conference on Turbulent Buoyant Convection*, pp. 361–372.

Noto, K., Teramoto, K. & Nakajima, T. 1999 Spectra and critical Grashof numbers for turbulent transition in a thermal plume. *J. Thermophys. Heat Transfer* **13**, 82–90.

Papanicolou, P. N. & List, E. J. 1988 Investigations of round vertical turbulent buoyant jets. *J. Fluid Mech.* **195**, 341–391.

Pham, M. V., Plourde, F. & Doan, K. S. 2005 Three dimensional characterization of a pure thermal plume. *J. Heat Transfer* **127**, 624–636.

Pham, M. V., Plourde, F. & Doan, K. S. 2006*a* Effect of swirl on pure turbulent thermal plume development. *Intl J. Heat Fluid Flow* **27**, 502–513.

Pham, M. V., Plourde, F., Doan, K. S. & Balachandar, S. 2006*b* Large-eddy simulation of a pure thermal plume under rotating conditions. *Phys. Fluids* **18**, 1–18.

Rooney, G. G. & Linden, P. F. 1996 Similarity considerations for non-Boussinesq plumes in an unstratified environment. *J. Fluid Mech.* **318**, 237–250.

Ricou, F. P. & Spalding, D. B. 1961 Measurements of entrainment by axisymmetrical turbulent jets. *J. Fluid Mech.* **11**, 21–32.

Shabbir, A. & George, W. K. 1994 Experiments on a round turbulent buoyant plume. *J. Fluid Mech.* **275**, 1–32.

da Silva, C. B. & Métais, O. 2002 On the influence of coherent structures upon interscale interactions in turbulent plane jets. *J. Fluid Mech.* **473**, 103–145.

Stanley, S. A., Sarkar, S. & Mellado, J. P. 2001 A study of the flow field evolution and mixing planar turbulent jet using direct numerical simulaiton. *J. Fluid Mech.* **450**, 377–407.

Soteriou, M. C., Dong, Y. & Cetegen, B. M. 2002 Lagrangian simulation of unsteady near field dynamics of planar buoyant plumes. *Phys. Fluids* **14**(9), 3118–3140.

Sreenivas, K. R. & Prasad, A. K. 2000 Vortex-dynamics model for entrainment in jets and plumes. *Phys. Fluids* **12**(8), 2101–2107.

Taylor, G. 1958 Flow induced by jets. *J. Aerospace Sci.* **25**, 464–465.

Turner, J. S. 1969 Buoyant plumes and thermals. *Annu. Rev. Fluid Mech.* **1**, 29–44.

Urbin, G. & Métais, O. 1997 Large-eddy simulations of three-dimensional spatially-developing round jets. *Direct and Large-Eddy Simulations II* (ed. J. P. Chollet, P. R. Voke & L. Kleiser. Kluwer).

Zhou, J., Adrian, R. J., Balachandar, S. & Kendall, T. M. 1999 Mechanisms for generating coherent packets of hairpin vortices in channel flow. *J. Fluid Mech.* **387**, 353–396.

Zhou, X., Luo, K. H. & Williams, J. J. R. 2000 Large-eddy simulation of a turbulent forced plume. *Eur. J. Mech.* B/*Fluids*, **20**, 233–254.